

Fluid-induced rupture experiment on Fontainebleau sandstone: Premonitory activity, rupture propagation, and aftershocks

A. Schubnel,^{1,2} B. D. Thompson,¹ J. Fortin,² Y. Guéguen,² and R. P. Young¹

Received 27 June 2007; accepted 22 August 2007; published 10 October 2007.

[1] A 14% porosity Fontainebleau sandstone sample (diameter = 40 mm, length = 88 mm) was loaded tri-axially, under 100 MPa confining pressure and 240 MPa differential stress. In drained conditions and under constant load, pore pressure (water) was raised until failure was triggered. During the experiment, elastic wave velocities and permeability were monitored while more than 3000 Acoustic Emissions (AE) were located prior and after failure. AE locations show that macroscopic fracture propagated from a large nucleation patch at speeds comprised between 0.1 and 4 m/s. **Number of AE hits per second followed Omori's law, with exponents of 0.92 and 1.18 pre- and post-failure respectively.** No quiescence was observed post failure, except where rupture initially nucleated from. Fast depressurization of the pore space induced secondary aftershocks located within the fracture plane, possibly indicating a heterogeneous fault geometry after rupture, of lower permeability, that compacted during the release of pore pressure. **Citation:** Schubnel, A., B. D. Thompson, J. Fortin, Y. Guéguen, and R. P. Young (2007), Fluid-induced rupture experiment on Fontainebleau sandstone: Premonitory activity, rupture propagation, and aftershocks, *Geophys. Res. Lett.*, 34, L19307, doi:10.1029/2007GL031076.

1. Introduction

[2] The generation and maintenance of pore pressure are of particular importance in crustal dynamics as they play a major role in the diagenetic cycle of sedimentary rocks, the production and ascension of volcanic lavas, aseismic deformation as well as within the earthquake cycle. In nature, numerous mechanisms exist which can give rise to the generation of pore overpressures: for example, porosity reduction [Wong *et al.*, 1997], thermal pressurization [Andrews, 2002], degassing or dehydration reactions [Dobson *et al.*, 2002]. Recent work on fault gouge mechanics have highlighted the crucial importance of the coupled evolution between damage, rock physical properties (e.g. wave velocities or permeability), temperature, pore pressure and solid stress [Rice, 1992]. In such way, in drained conditions that are characteristic of Earth's crust, the development of pore pressure excess is profoundly influenced by the spatial and temporal variations of permeability [Miller, 2002]. For example, the coupling between strain rate and permeability can lead to cases where, on the small scale, rocks are not fully drained thus leading to localized pore fluid pressure excess [Brace and

Martin, 1968]. Evidence of pore-pressure driven aftershocks [Shapiro *et al.*, 2003; Miller *et al.*, 2004] and long distance triggering in geothermal areas [Kanamori and Brodsky, 2004] have also emphasized the role fluids may play in the redistribution of normal stresses [Koerner *et al.*, 2004] and earthquake triggering. But the complications associated with in-situ monitoring of crustal pore pressures in natural fault zones is such that little is known quantitatively on the acoustic (or seismic) signatures of varying fluid pressures in the field, which are nevertheless thought to play a crucial mechanical (and chemical) role.

[3] In the laboratory however, many Acoustic Emission (AE) studies have documented the mechanics of failure propagation in dry rocks [Lockner, 1993] or dry fault gouge analogues [Mair *et al.*, 2007]. In the presence of fluid, AE studies have been performed: (1) in drained conditions at constant pore pressure, on the water weakening effect due to stress corrosion processes in sandstones [Baud and Meredith, 1997, 2000], damage accumulation and mapping [Zang *et al.*, 1996], shear and compaction band formation [Fortin *et al.*, 2006; Benson *et al.*, 2007], and the strain rate and temperature dependence of Omori's law exponent [Ojala *et al.*, 2004]; (2) in undrained conditions, several studies have concentrated on dehydrating rocks such as serpentinite [Dobson *et al.*, 2002] or gypsum [Milsch and Scholz, 2005] while Schubnel *et al.* [2006] have recently investigated aseismic failure of marble due to pore pressurization. In this preliminary study, we have investigated experimentally the mechanical role an increasing pore pressure plays on AE triggering and fracture propagation in drained conditions on a high permeability sandstone.

2. Experimental Set-Up and Procedure

[4] A Fontainebleau sandstone specimen (length = 88 mm, diameter = 40 mm; cored perpendicular to the bedding plane) was deformed inside a triaxial vessel installed at the Laboratoire de Géologie of Ecole Normale Supérieure in Paris, France [Fortin *et al.*, 2005; Schubnel *et al.*, 2005]. This triaxial cell of low stiffness is equipped to record axial, radial and volumetric strains, permeability along the vertical axis and acoustic activity contemporaneously. A network of 14 piezoceramic transducers (PZT) was used in order to measure P wave velocities along several directions and locate AE during the experiment. Absolute velocities were calculated with an error bar of a few percent but relative error was lowered to 0.5% using cross-correlation and double picking techniques. AE were captured using a unique and innovative instrument [Thompson *et al.*, 2005, 2006], which stores continuous ultrasonic waveform data onto a 40 GB circular Random Access Memory (RAM) buffer with 14-bit resolution. This

¹Lassonde Institute, University of Toronto, Toronto, Ontario, Canada.

²Laboratoire de Géologie, Ecole Normale Supérieure, Paris, France.

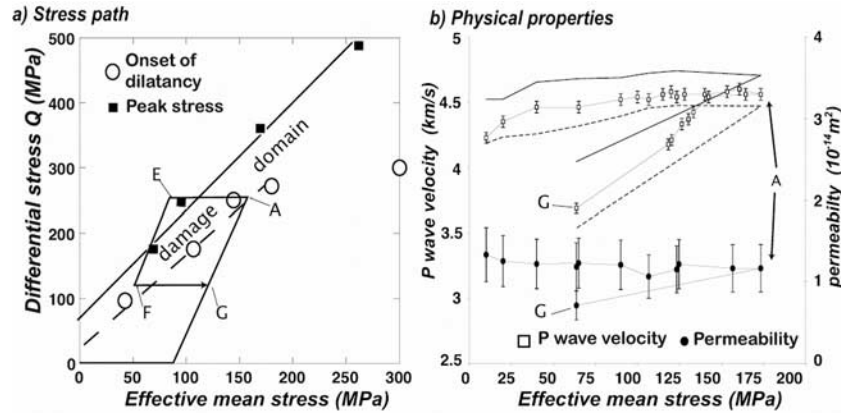


Figure 1. (a) Mechanical envelope of Fontainebleau sandstone (onsets of dilatancy and peak stresses). The arrow shows the stress path followed during this experiment (*A*, water injection phase; *E*, rupture; and *G*, pore pressure release). (b) Physical properties as a function of effective mean stress. Averaged, vertical (upper dashed line), and horizontal P wave velocities are represented. Filled circles show the averaged (upstream and downstream) permeability measurements.

system was designed in response to the limitation of existing AE acquisition systems so that here, the complete AE catalog could be recorded at a very high resolution (10 MHz sampling frequency). The RAM was frozen a few seconds after macroscopic rupture. The continuous acoustic data was then downloaded and harvested for discrete AE events. AE absolute source locations were obtained with an average accuracy of ± 2 mm, using a homogeneous transversely isotropic velocity profile (fast vertical P wave velocity - initially 4250 m/s, and then calibrated again after each velocity survey, anisotropy factor 5%) and a Downhill Simplex algorithm [Nelder and Mead, 1965].

[5] Inside the vessel, the sample was covered with a Neoprene jacket. Axial strain and stress were measured using a strain gage glued directly onto the sample (strain measurement accuracy was $\sim 10^{-6}$), an internal load cell placed on top of the sample (relative stress measurement accuracy was ~ 0.1 MPa) and a LVDT placed on top of the piston (total displacement accuracy ~ 10 μ m). Pore pressure was driven by two precision volumetric pumps and distilled water was introduced into the sample through hardened steel end pieces and porous spacers located on the top and bottom of the rock sample. The sample was saturated for 24 hours prior to the experiment and then deformed under fully drained conditions. At various points, the experiment was stopped and permeability measurements were per-

formed in both directions (upstream and downstream) along the main axis of compression, using a continuous delta pressure technique (1 MPa) and measuring the continuous resulting flow (between 30–300 cm³/hr) provided by the two servo-controlled pumps.

3. Experimental Results

3.1. Stress Path, Physical Properties, and Acoustic Activity

[6] Figure 1a presents the mechanical envelope of this 14% porosity Fontainebleau sandstone. Onset of inelastic dilatant deformation (dilatancy - circles) and peak strength stresses (squares) were measured in drained conditions on samples all coming from the same block. The space limited by these two lines correspond to the so-called damage domain, i.e. the domain where crack propagation takes place. Below the onset of dilatancy, deformation is purely elastic (or visco-elastic). On Figure 1a, the arrow shows the stress path followed as a function of differential stress $[\sigma_1 - \sigma_3]$ and effective mean stress $[(\sigma_1 + 2\sigma_3)/3 - P_p]$, where σ_1 is the vertical compressive stress, σ_3 the confining pressure and P_p the pore pressure. This particular stress path was chosen so that the sample crossed the damage domain by pore pressurization solely. The sample was initially loaded within the elastic domain (point noted *A* on Figures 1 and 2): confining P_c and pore pressure P_p were set to 100 MPa and 10 MPa

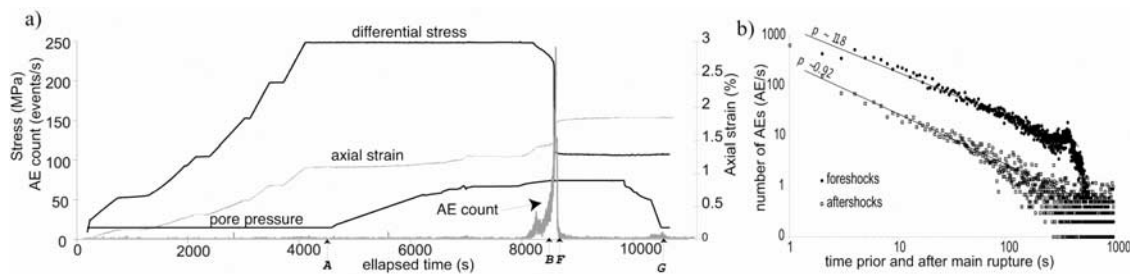


Figure 2. (a) Differential stress, pore pressure, axial strain, and acoustic activity (number of AE per second) versus elapsed time during the experiment. *A* (pore pressure increase), *G* (pore pressure release), *B* and *F* (start and end of the continuous record on Figure 3a) are indicated by arrows. (b) Number of fore- and aftershocks were a power law function of time, with Omori exponents of ~ 0.92 and ~ 1.18 prior and after failure respectively.

respectively while differential stress was raised to 240 MPa. The sample was then brought back at constant differential stress into the brittle field by increasing the pore pressure solely and thus reducing the effective mean stress. At a pore pressure of 62 MPa, brittle failure was triggered (*E*) and the stress suddenly dropped to (*F*). Once quiescence was reached, pore pressure was completely released (*G*).

[7] Figure 1b shows the contemporaneous evolution of physical properties (P wave velocities and permeability) as a function of effective mean stress. The empty symbol displays the mean (averaged) P wave velocity, while the dashed lines represent the mean upper (vertical) and lower (horizontal) values of P wave velocity. Initially, P wave velocities were equal to ~ 4.25 km/s. The rock showed a 5% anisotropy, with vertical velocities being faster than horizontal ones. Initial permeability along the compressive axis was equal to $\sim 1.25 \times 10^{-14}$ m². Permeability and velocity evolutions were highly correlated throughout the experiment. Initially, elastic compaction was accompanied with an increase in P wave velocity and a slight decrease of permeability, probably due to visco-elastic crack closure. During this elastic phase, very few AEs were detected (Figure 2). Beyond *A* and as the pore pressure increased further, no hysteresis was observed for P wave velocities, which decreased with decreasing effective mean stress due to poro-elastic deformation (and crack re-opening). Further on, P wave velocities started to decrease substantially, as a consequence of microcracking. This also corresponded to an increase in P wave anisotropy, a decrease in permeability and the onset of AE triggering (Figure 2), the rate of which reached a peak at failure. After failure, the final bulk permeability of the rock sample was lower than the initial one, which can be explained by the fact the fault plane may have exhibited a much reduced permeability due to grain crushing and gouge production [Zhu and Wong, 1997; Fortin et al., 2005], while the rest of sample probably had a slightly larger permeability due to the reduction of effective mean stress as a result of the stress drop.

[8] Figure 2 displays the contemporaneous evolution of stress (differential stress and pore pressure), axial strain and acoustic activity (number of detected AEs per second). Brittle failure was attained at $P_p = 62$ MPa, with an associated differential stress drop of 140 MPa. The amount of slip, measured using a LVDT placed on top of the sample and resolved for a 60° dipping fracture plane, was ~ 0.3 mm. This yields a seismic moment M_0 (calculated as $M_0 = \mu A u$, with a shear modulus $\mu = 20$ GPa, a fault area, $A = 30$ cm² and u as the measured slip) equal to 1.7×10^4 Nm, which corresponds to a moment magnitude M_w (calculated using $M_w = 2/3 \log_{10} M_0 - 6.0$) of -3.2 . Failure nucleation and rupture propagation were accompanied by a peak of acoustic activity reaching up to 1000 per second for a few seconds. After rupture, the AE rate decreased until quasi-quiescence. However, the final pore depressurization (noted *G* on Figure 2) unexpectedly induced a second set of aftershocks, probably due to local P_p re-equilibrations on the fault plane and the fault zone lower permeability. Figure 2b plots the number of foreshocks and aftershocks as a function of logarithmic time. Regression lines show that both datasets follow a power law (Omori's law), with exponents of ~ 0.92 and ~ 1.18 pre- and post-failure respectively. This is comparable to values Ojala et al.

[2004] observed on drained sandstones experimentally as well as values generally observed in the field [Helmstetter, 2002].

3.2. AE Locations, Nucleation Patch, Rupture Velocity and Aftershocks

[9] Figure 3a displays a 134 second continuous acoustic waveform, sampled at 10 MHz, over the course of rupture, and the contemporaneous evolution of differential stress and axial strain superimposed. Similar continuous waveforms of all 14 PZT sensors were harvested for discrete AE events and chopped into time periods from *B* to *F*. In this experiment, frictional slip and stress drop were short phases ($EF < 1$ s) that clearly corresponds to a peak of acoustic activity. Figure 3b displays a zoom of the time period *EF*. Between the dashed lines, AEs were triggered too rapidly to distinguish discrete events. In consequence, few AEs could be located during this critical time period (~ 0.25 s). During these 0.25 s, the sensors were also fully saturated in voltage during ~ 5 ms, as indicated on Figure 3b.

[10] Over 3 000 AEs were located and Figure 3b displays the AE locations from *A* to *G*. During the time period *AB* (~ 1 h), 832 events were located and demonstrate the early stages of strain localization. Within that first hour, and as the pore pressure was slowly raised, only few AE located in the bulk volume of the specimen. It might be that some pre-existing heterogeneities might have controlled the initiation of strain localization in the upper left of the specimen, as seen by Lei et al. [2004] in granite or Fortin et al. [2006] in sandstone. In the time period *BC* ~ 50 s, AEs clustered in a cloud. The cluster of AEs got smaller as the density of AEs in its center increased, demonstrating the initiation of a nucleation patch. Within the AE cluster, the final AE density (total number of AE hits in the volume) reached ~ 850 AE/cm³ at rupture. Approximately 1/4 of the total number of AEs located within 1 cm³ of the sample, highlighting the extensive damage occurring within the nucleation zone prior to failure. During the time periods *CD* = 30 s and *DE* = 10 s, the nucleation patch accelerated from a few tenths of mm.s⁻¹ to a few mm.s⁻¹, so that at during time period *DE*, the strain rate was already increasing rapidly and the stress started to drop. Within the next second (time period *EF*), unstable failure propagated through the entire sample. Unfortunately, only a few AEs could be located within time period *EF*, as the AE rate was too fast to distinguish distinct AE events. However, most AEs occurring before the first dashed line on Figure 3b locate inside the nucleation patch. AEs occurring after the second dashed line in Figure 3b also locate at the base of the fault plane. Therefore, the region highlighted on Figure 3c (a large asperity of ~ 2 cm radius) failed within ~ 0.25 s during which no AEs could be located. This yields a lower bound for the rupture velocity of the order of 0.1 m.s⁻¹. Assuming that the period of full saturation of the sensors (5 ms) corresponds to the actual dynamic propagation of the failure in the asperity also yields an upper bound for the rupture velocity of 4 m.s⁻¹. Unlike in dry AE experiments, quiescence was not reached before an hour after rupture and a large number of aftershocks were observed. More than 200 AEs were located in the time period *FG*, revealing a relative lack of activity where rupture initially nucleated (highlighted by the

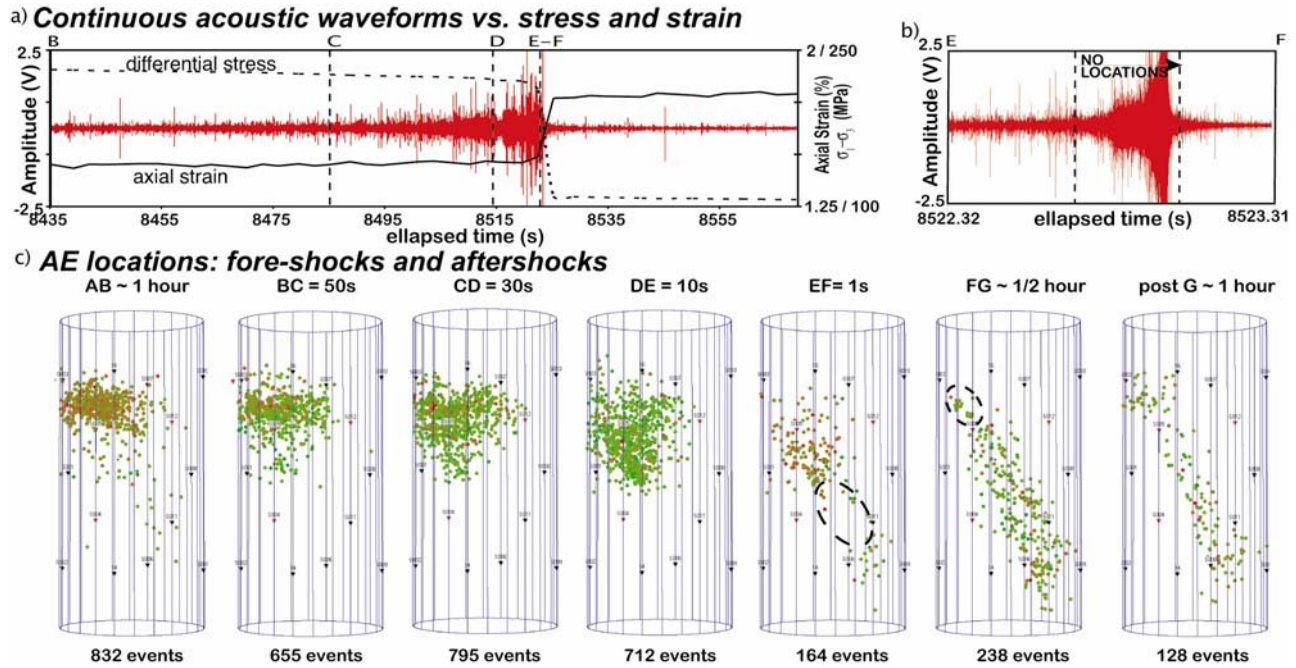


Figure 3. (a) Stress, strain, and radiated acoustic energy. A 134 second segment of the continuous acoustic waveform recorded on one single channel over the course of rupture. The evolution of axial strain and shear stress are also displayed, which is chopped into time periods, starting from *B* to *F*. (b) Zoom-in on time period *EF*. No AE locations could be performed between the dashed lines. (c) AE locations during time periods *AB*, *BC*, *CD*, *DE*, *EF*, *FG*, and after *G*.

ellipse). This could be explained by the important premonitory activity within this region. Unfortunately, no conclusive microstructural analysis was performed to support this hypothesis. Finally and once quiescence was reached, the final release of pore pressure (*G*) also triggered a set of aftershocks, all located within the fault zone. It is likely that these aftershocks were triggered by differential pore pressure effects due to differential permeability along and across the fault plane.

4. Discussions and Conclusions

[11] In this preliminary study, three phases were observed during the rupture of an intact Fontainebleau sandstone specimen by pore pressurization. The first one corresponded to clustered premonitory acoustic activity and strain localization. During this phase, elastic wave velocities and permeability were affected and decreased, due to micro-cracking. The second phase corresponded to the initiation of a nucleation patch on which slip accelerated up to speeds of \sim mm/s. Unstable rupture propagated in less than 0.25 s at speeds between 0.1–4 m/s. During this period, AEs were triggered so rapidly that distinct AE events could not be distinguished anymore. This raises the fundamental question of the nature of the waveforms acoustically radiated during rupture propagation: can the sum of 1000 AEs, corresponding to crack propagation increments of a few tens of microns, be considered as one large event, corresponding to the fracture of an asperity of a few centimeters in size? Our experimental observations, which tend to answer positively to this question, are also in close agreement with previous laboratory experiments [Thompson *et al.*, 2006] and field scale injection experiment studies

[Shapiro *et al.*, 2006]. It also seem to follow, qualitatively at least, the trends of Ohnaka's [2003] theoretical model of unstable rupture nucleation both in intact and non-cohesive rock materials, in which the nucleation size scales with the amount of final slip and the rupture velocity evolves from stable (or quasi-static) during a nucleation phase to unstable (or dynamic) during the propagation phase. In our experiment, the critical rupture velocity seems to be the order of a few mm.s^{-1} , before fast acceleration of the fracture speed. The third phase of our experiments corresponded to aftershock triggering, which revealed a relative lack of activity within the rupture nucleation zone. This might be due to the extensive premonitory damage accumulation within this region (up to 850 AE within 1 cm^3) where the stress heterogeneities might have already been extensively released prior to failure. Aftershock distribution in time followed a power law decrease (Omori's exponent of 1.18). Secondary aftershocks might have been due to the (1) possible fault heterogeneous geometry after rupture, and (2) the compaction of the fault plane which resulted in a decrease of the bulk permeability. Several experiments of the same kind are now being planned on different rock type to help built a catalog of the acoustic signature of rocks during failure nucleation, and aftershock time patterns.

[12] **Acknowledgments.** The authors would like to thank P.M. Benson, M.H.B. Nasser and D.S. Collins. We would also like to thank Sergei Shapiro and Dan Faulkner for their highly constructive comments that greatly improved the quality of our manuscript. This project was funded via a National Environment Research Council (NERC) equipment grant, a Natural Sciences and Engineering Research Council of Canada (NSERC) Discovery Grant and the Fonds France Canada pour la Recherche (FFCR).

References

- Andrews, D. J. (2002), A fault constitutive relation accounting for thermal pressurization of pore fluid, *J. Geophys. Res.*, *107*(12), 2363, doi:10.1029/2002JB001942.
- Baud, P., and P. B. Meredith (1997), Damage accumulation during triaxial creep of Darley Dale sandstone from pore volumetry and acoustic emission, *Int. J. Rock Mech. Min. Sci.*, *34*, Pap. 024.
- Baud, P., W. L. Zhu, and T.-F. Wong (2000), Failure mode and weakening effect of water on sandstone, *J. Geophys. Res.*, *105*, 16,371–16,389.
- Benson, P. M., B. D. Thompson, P. G. Meredith, S. Vinciguerra, and R. P. Young (2007), Imaging slow failure in triaxially deformed Etna basalt using 3D acoustic-emission location and X-ray computed tomography, *Geophys. Res. Lett.*, *34*, L03303, doi:10.1029/2006GL028721.
- Brace, W. F., and R. J. Martin (1968), A test of the effective stress for crystalline rocks of low porosity, *Int. J. Rock Mech. Min. Sci. Geomech. Abstr.*, *5*, 415–426.
- Dobson, D. P., P. G. Meredith, and S. A. Boon (2002), Simulation of subduction zone seismicity by dehydration of serpentine, *Science*, *298*, 1407–1410.
- Fortin, J., A. Schubnel, and Y. Guéguen (2005), Elastic wave velocities and permeability evolution during compaction of Bleurswiller sandstone, *Int. J. Rock Mech. Min. Sci.*, *42*, 873–889.
- Fortin, J., S. Stanchits, G. Dresen, and Y. Guéguen (2006), Acoustic emission and velocities associated with the formation of compaction bands in sandstone, *J. Geophys. Res.*, *111*, B10203, doi:10.1029/2005JB003854.
- Helmstetter, A. (2002), Ruptures et instabilités: Similitude et mouvements gravitaires, Ph.D. thesis, 388 pp., Univ. Joseph Fourier, Grenoble, France.
- Kanamori, H., and E. E. Brodsky (2004), The physics of earthquakes, *Rep. Prog. Phys.*, *67*, 1429–1496.
- Koerner, A., E. Kissling, and S. A. Miller (2004), A model of deep crustal fluid flow following the $M_w = 8.0$ Antofagasta, Chile, earthquake, *J. Geophys. Res.*, *109*, B06307, doi:10.1029/2003JB002816.
- Lei, X.-L., L. Masuda, O. Nishizawa, L. Jouniaux, L. Liu, W. Ma, T. Satoh, and K. Kusunose (2004), Detailed analysis of acoustic emission activity during catastrophic fracture of faults in rocks, *J. Struct. Geol.*, *26*, 247–258.
- Lockner, D. A. (1993), The role of acoustic emission in the study of rock fracture, *Int. J. Rock Mech. Min. Sci.*, *30*, 1039–1046.
- Mair, K., C. Marone, and R. P. Young (2007), Rate dependence of acoustic emissions generated during shear of simulated fault gouge, *Bull. Seismol. Soc. Am.*, in press.
- Miller, S. A. (2002), Properties of large ruptures and the dynamical influence of fluids on earthquakes and faulting, *J. Geophys. Res.*, *107*(B9), 2182, doi:10.1029/2000JB000032.
- Miller, S. A., C. Collettini, L. Chiaraluce, M. Cocco, M. Barchi, and B. J. P. Kaus (2004), Aftershocks driven by a high-pressure CO_2 source at depth, *Nature*, *427*, 724–727.
- Milsch, H. H., and C. H. Scholz (2005), Dehydration-induced weakening and fault slip in gypsum: Implications for the faulting process at intermediate depth in subduction zones, *J. Geophys. Res.*, *110*, B04202, doi:10.1029/2004JB003324.
- Nelder, J., and R. Mead (1965), A simplex method for function minimisation, *Comput. J.*, *7*, 308–312.
- Ojala, I. O., I. G. Main, and B. T. Ngwenya (2004), Strain rate and temperature dependence of Omori law scaling constants of AE data: Implications for earthquake foreshock-aftershock sequences, *Geophys. Res. Lett.*, *31*, L24617, doi:10.1029/2004GL020781.
- Ohnaka, M. (2003), A constitutive scaling law and a unified comprehension for frictional slip failure, shear fracture of intact rock, and earthquake rupture, *J. Geophys. Res.*, *108*(B2), 2080, doi:10.1029/2000JB000123.
- Rice, J. R. (1992), Fault stress states, pore pressure distributions and the weakness of the San Andreas fault, in *Fault Mechanics and Transport Properties of Rocks*, edited by B. Evans and T.-F. Wong, pp. 475–503, Academic, London.
- Schubnel, A., J. Fortin, L. Burlini, and Y. Guéguen (2005), Damage and recovery of calcite rocks deformed in the cataclastic regime, in *High Strain Zones: Structures and Physical Properties*, edited by D. Bruhn and L. Burlini, pp. 203–221, Geol. Soc., London.
- Schubnel, A., E. Walker, B. D. Thompson, J. Fortin, Y. Guéguen, and R. P. Young (2006), Transient creep, aseismic damage and slow failure in Carrara marble deformed across the brittle-ductile transition, *Geophys. Res. Lett.*, *33*, L17301, doi:10.1029/2006GL026619.
- Shapiro, S. A., R. Patzig, E. Rothert, and J. Rindschwentner (2003), Triggering of seismicity by pore-pressure perturbations: Permeability-related signatures of the phenomenon, *Pure Appl. Geophys.*, *160*, 1051–1066.
- Shapiro, S. A., C. Dinske, and E. Rothert (2006), Hydraulic-fracturing controlled dynamics of microseismic clouds, *Geophys. Res. Lett.*, *33*, L14312, doi:10.1029/2006GL026365.
- Thompson, B. D., R. P. Young, and D. A. Lockner (2005), Observations of premonitory acoustic emission and slip nucleation during a stick slip experiment in smooth faulted Westerly granite, *Geophys. Res. Lett.*, *32*, L10304, doi:10.1029/2005GL022750.
- Thompson, B. D., R. P. Young, and D. A. Lockner (2006), Observations of fracture in Westerly granite under AE feedback and constant strain rate loading: Nucleation, quasi-static propagation, and the transition to unstable fracture propagation, *Pure Appl. Geophys.*, *163*, 995–1019.
- Wong, T.-F., C. David, and W. Zhu (1997), The transition from brittle faulting to cataclastic flow in porous sandstones: Mechanical deformation, *J. Geophys. Res.*, *102*, 3009–3025.
- Zang, A., C. F. Wagner, and G. Dresen (1996), Acoustic emission, microstructure, and damage model of dry and wet sandstone stressed to failure, *J. Geophys. Res.*, *101*, 17,507–17,521.
- Zhu, W., and T.-F. Wong (1997), The transition from brittle faulting to cataclastic flow: Permeability evolution, *J. Geophys. Res.*, *102*, 3027–3041.

J. Fortin, Y. Guéguen, and A. Schubnel, Laboratoire de Géologie, Ecole Normale Supérieure, 24 Rue Lhomond, F-75005 Paris, France. (aschubnel@geologie.ens.fr)

B. D. Thompson and R. P. Young, Lassonde Institute, University of Toronto, 170 College Street, Toronto, ON, Canada M5S 3E3.